Bioorganic & Medicinal Chemistry 23 (2015) 1112–1122

Contents lists available at ScienceDirect

Bioorganic & Medicinal Chemistry

journal homepage: www.elsevier.com/locate/bmc

Radiosynthesis and micro-SPECT analysis of triazole-based RGD integrin ligands as non-peptide molecular imaging probes for angiogenesis

Francesca Bianchini [a,†], Pierangelo Fabbrizzi [b,†], Gloria Menchi [b,c], Silvia Raspanti [d], Anna Bottoncetti [e], Alessandro Passeri [c,d], Elena Andreucci [a], Antonio Guarna [b,c], Lido Calorini [a,*], Alberto Pupi [c,d,e,*], Andrea Trabocchi [b,c,*]

[a] Department of Clinical and Experimental Biomedical Science 'Mario Serio', University of Florence, Viale Morgagni 50, 50134 Florence, Italy
[b] Department of Chemistry 'Ugo Schiff', University of Florence, Via della Lastruccia 13, 50019 Sesto Fiorentino, Florence, Italy
[c] Interdepartmental Center for Preclinical Development of Molecular Imaging (CISPIM), University of Florence, Viale Morgagni 85, 50134 Florence, Italy
[d] Department of Clinical and Experimental Biomedical Science 'Mario Serio', University of Florence, Largo Brambilla 3, 50134 Florence, Italy
[e] Azienda Ospedaliera Universitaria Careggi (AOUC), Largo Brambilla 3, 50134 Florence, Italy

ARTICLE INFO

Article history:
Received 11 October 2014
Revised 22 December 2014
Accepted 28 December 2014
Available online 13 January 2015

Keywords:
Integrins
Molecular imaging
Cancer
Angiogenesis
Amino acids

ABSTRACT

Taking advantage of click chemistry, we synthesized triazole-containing RGD peptidomimetics capable of binding to $\alpha_v\beta_3$ integrin with diverse potency, and selected ^{125}I-labeled compounds proved to interact in vitro and in vivo with $\alpha_v\beta_3$ integrin expressed by melanoma cells. Two ^{125}I-compounds containing either 2-aminobenzimidazole or 2-aminopyridine groups as the arginine bioisostere with the capacity to selectively bind cells of highly expressing $\alpha_v\beta_3$ melanoma xenografts were found using micro-SPECT imaging studies.

1. Introduction

During the last decade medical imaging technologies experienced a remarkable growth, and nowadays occupy a central function in clinical oncology.[1] In this view, the use of biomarkers for molecular imaging in pre-clinical studies has been proven useful in accelerating the development of targeted cancer therapies. Among all molecular imaging techniques, positron emission tomography (PET) and single-photon emission computed tomography (SPECT) played an increasing role in pre-clinical investigations, taking advantage of the high sensitivity and the specificity of these approaches.[2] Indeed, molecular imaging studies using radiopharmaceuticals are oriented towards receptor-based studies,[3,4] because this approach is helpful in confirming the mechanism of action at the molecular level and in obtaining information such as receptor density and occupancy.[5,6] Promising anti-angiogenic treatments for cancer therapy have become well-established in recent years. Angiogenesis, consisting of the generation of new capillaries from existing blood vessels, is a common process associated to several pathological processes, including the growth of tumor tissues. Angiogenesis is a multistep process in which the proteolytic degradation of the basal membrane allows for loosening the endothelial cells adhesion and their proliferation and migration. Final re-adhesion of newly-formed endothelial cells gives rise to new capillary vessels. Anti-angiogenic therapy is fundamental in blocking endothelial cells growth and inducing their necrosis, resulting in the reduced endothelial network to starve the tumor mass in term of nutrient and oxygen supply.

Integrins are transmembrane heterodimeric glycoprotein receptors consisting of various combinations of α and β subunits. These receptors regulate many important biological processes such as cell adhesion, migration and invasion, cell growth and differentiation, and apoptosis. The role of integrins in the regulation of angiogenesis is an essential feature in tumor progression and metastatic dissemination.[7–10] As biomarkers for molecular imaging of

* Corresponding authors. Tel.: +39 055 4598207; fax: +39 055 4598900 (L.C.); tel.: +39 055 7947527; fax: +39 055 4224392 (A.P.); tel.: +39 055 4573507; fax: +39 055 4574913 (A.T.).
E-mail addresses: lido.calorini@unifi.it (L. Calorini), a.pupi@dfc.unifi.it (A. Pupi), andrea.trabocchi@unifi.it (A. Trabocchi).
† These authors contributed equally to the work.

http://dx.doi.org/10.1016/j.bmc.2014.12.065
0968-0896/

angiogenesis are needed to monitor the progress of the therapeutic treatment at the molecular level, efforts have been dedicated to integrins as selective targets in molecular imaging approaches to set up tailored anti-angiogenic treatments. Accordingly, several in vivo imaging probes for PET and SPECT, for optical imaging, and for magnetic resonance imaging (MRI) have been developed.[11] Cilengitide is a RGD (arginine–glycine–aspartic acid) mimetic integrin inhibitor representing a relevant entry in the panorama of molecular imaging agents for defining new tumor therapies. Although a number of RGD peptidomimetics have been reported in the literature,[12–15] much effort has been focused on the application of Cilengitide as a chemical probe for the molecular imaging of angiogenesis.

Our previous contribution in this field consisted of developing a Cilengitide-like RGD cyclopentapeptide containing the cyclic amino acid (*R*)-morpholine-3-carboxylic acid,[16,17] and the successful evaluation of this molecule as a ^{125}I-labeled SPECT imaging agent for angiogenesis in a melanoma xenograft murine model.[18] In view of advancing the in vivo study of RGD radioligands, we became interested in small molecule radiotracers possessing a non-peptide character. Accordingly, we recently reported the synthesis and integrin binding evaluation of triazole peptidomimetics of the RGD sequence by means of copper-catalyzed azide–alkyne cycloaddition (CuAAC).[19] One compound of this class showed high binding capacity for $\alpha_v\beta_3/\alpha_v\beta_5$ integrins, thus we envisaged the application of this molecule as a novel molecular imaging agent by exploring diverse positions for labeling with ^{125}I radioisotope. The use of ^{125}I for pre-clinical molecular imaging studies is of special interest, because it is a readily available radionuclide commonly used in molecular biology, and many ^{125}I-labeled radiopharmaceuticals are commercially available. Also, iodine-labeled compounds represent a valuable tool for translating pre-clinical results up to humans because the substitution of ^{125}I with ^{123}I provides a probe suitable for SPECT imaging in humans. Furthermore, molecular imaging by PET can be accomplished with the positron emitter ^{124}I, and the translation to the radionuclide therapy using ^{131}I (emitting β- and γ-rays) can be easily assessed.

In this work, we report the modification of compound **1** (Fig. 1) by replacing the phenyl ring with a phenol group or by alkylating the guanidine moiety with a tyramine appendage, in order to introduce an iodine atom on the aromatic ring. This project was undertaken with the aim of assessing whether these RGD peptidomimetics, appropriately labeled, could be suitable for SPECT/PET molecular imaging using iodine radionuclides and in order to explore the structure–activity relationship of the compounds in vivo. The study was conceived by modulating the arginine bioisostere and the position of the radioisotope, namely on the aromatic ring of the azide fragment or using a tyramine moiety installed on the guanidine group. The modulation of the guanidine bioisostere was studied to understand the role of such chemical moiety in some in vitro biological characteristics of tumor cells directed by integrins and in the pharmacokinetics and pharmacodynamics profile of the radioligand.

2. Results and discussion

2.1. Synthesis

Triazole-based RGD ligands were achieved by combining azides and alkynes (see Supplementary data for their preparation) in the Cu-catalyzed azide–alkyne cycloaddition, followed by acid-mediated hydrolysis of the protecting groups of side chain isosteres (Schemes 1 and 2). $CuP(OEt)_3I$ proved to work smoothly in the Cu-catalyzed reaction, as compared to previous application of other copper salts,[19] resulting in the preparation of side-chain protected (Pg) RGD mimetics **Pg-6**–**Pg-9** in 55–89% yields. Subsequent deprotection in 3 M HCl furnished the corresponding RGD mimetics **6**–**9** in pure form. The synthesis of compound **7** (Scheme 1) required a different hydrolysis procedure, as the treatment with 3 M HCl resulted in product degradation. Specifically, the removal of the protecting groups was achieved using a 1:1 mixture of

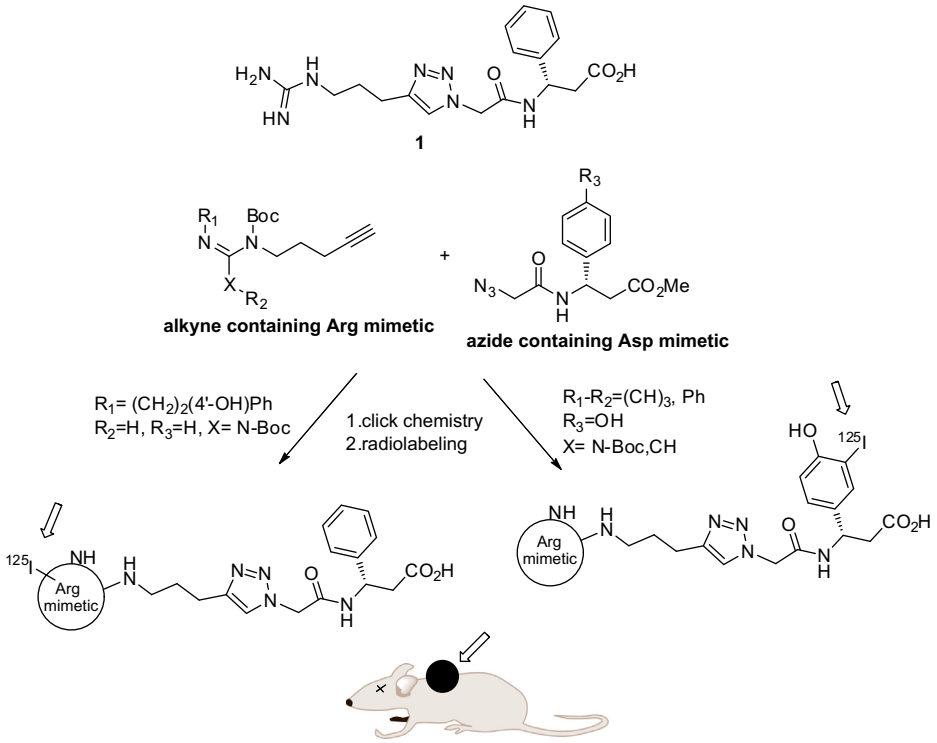

Figure 1. Design of RGD peptidomimetic ligands as SPECT imaging probes containing ^{125}I.

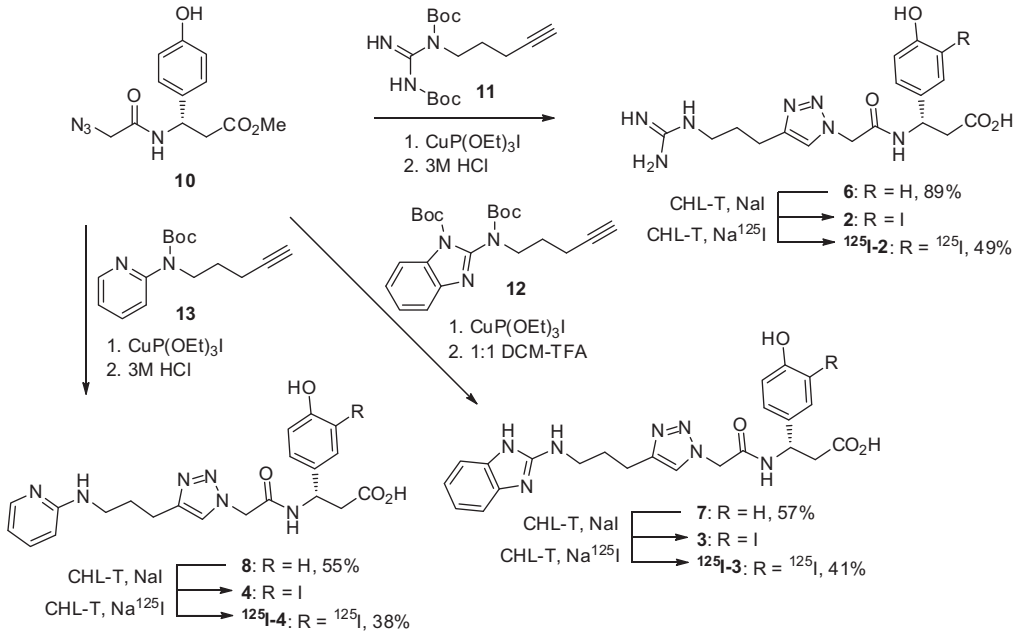

Scheme 1. Synthetic approach for RGD mimetic radioligands **2**–**4** containing either guanidine or its bioisosteres.

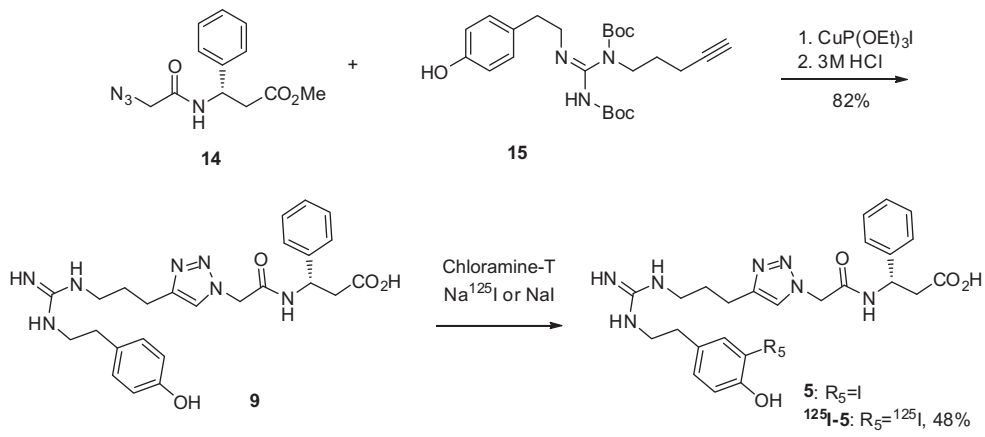

Scheme 2. Synthetic approach for the RGD mimetic radioligand **5** containing the tyramine linkage.

TFA–dichloromethane instead of an aqueous system, resulting in a clean hydrolysis to give **7**.

The iodination procedure consisted of the direct labeling with NaI (1:1 molar ratio) using chloramine-T (CHL-T) as the oxidizing reagent in a phosphate buffered saline solution (PBS). The reaction was quenched with sodium metabisulfite, and the crude product was purified by semipreparative HPLC to give the corresponding iodinated compounds **2**–**5** in pure form. The same approach was then applied for radiolabeling using $Na^{125}I^{125}I$ in 1:18 molar ratio with respect to RGD mimetic precursors **6**–**9** to favor the monoiodination. The crude reaction mixture was purified by HPLC, and the fractions were collected through radioactivity monitoring with a γ-counter, resulting in a clean iodination reaction with a radiochemical yield of 38–49% for compounds ^{125}**I-2**–^{125}**I-5**.

2.2. Integrin binding assays

Solid-phase assays were applied to test the ability of RGD peptidomimetics **6**–**9** and their corresponding iodinated compounds **2**–**5** to compete with ^{125}I-echistatin for binding to pure $\alpha_v\beta_3$ integrin (Table 1).[19] IC_{50} values showed all iodinated compounds possessing a higher binding affinity toward $\alpha_v\beta_3$ integrin as compared to their corresponding precursors. The $\alpha_v\beta_3$ inhibition curves of all RGD mimetics but **6**, **2** and **3** were better described by a two-sites model (Table 1), as showed by Hill slope values different from unity, as a consequence of binding of the peptidomimetic compound with two conformational states of integrins, in agreement with other ligands already reported in the literature.[20–24] Compound **6** and its iodinated analogue **2** showed a one-site binding profile and binding affinity in the low micromolar range (2.1 and 0.66 μM, respectively). Compounds **3** and **4**, proved to bind to $\alpha_v\beta_3$ integrin with higher affinity in the nanomolar range and according to a one-site and two-sites models, respectively, suggesting an important role of the guanidine isostere towards binding activity. Compounds **9** and **5** showed divergent ligand capacity, as the former demonstrated poor binding to $\alpha_v\beta_3$ integrin, and the latter good binding to the high-affinity conformation but quite poor binding to the low-affinity conformational state of $\alpha_v\beta_3$ integrin. These results suggested that alkylation of the guanidine group produced a significant modification of the binding affinity towards $\alpha_v\beta_3$ integrin as

Table 1
Inhibition of ^{125}I-echistatin specific binding to purified human integrin proteins $\alpha_v\beta_3$ by triazole-containing RGD peptidomimetics **6–9** (right) and their corresponding iodinated derivatives (**2–5**)

Iodinated Compd	IC_{50}	Hill coeff.	Compd	IC_{50}	Hill coeff.
1	High: 16.4 ± 5.3 nM Low: 3.4 ± 1.6 μM	−0.38	—	—	—
6	2.1 ± 1.3 μM	−0.79	**2**	660 ± 110 nM	−1.56
7	37 ± 11 nM	−0.75	**3**	64 ± 11 nM	−0.96
8	N/A (100% inhib. at 10 μM 86% inhib. at 1.0 μM)	—	**4**	High: 0.21 ± 0.16 nM Low: 630 ± 110 nM	−0.57
9	High: 310 ± 220 nM Low: no convergence	−0.25	**5**	High: 41 ± 12 nM Low: 55 ± 12 μM	−0.16

Binding data of compound **1** are added as a reference[a].
[a] High and low IC_{50} values refer to two-sites binding model.

compared to the introduction of the other moieties as found in compounds **2–4**, resulting in a switch of binding affinity from nano- to micromolar range for tyramine-containing RGD mimetics. This binding affinity profile was further confirmed by cell adhesion assays.

2.3. Cell biology assays

The candidate RGD peptidomimetic ligands were tested for their integrin binding affinity towards M21 human melanoma cells. Cytofluorimetric analysis revealed that M21 human melanoma cells express high levels of $\alpha_v\beta_3$ integrin heterodimer (92–95% positive cells) and low levels of $\alpha_v\beta_5$ integrin heterodimer (25–28% positive cells) (data not shown). We demonstrated the capacity of RGD peptidomimetics **6–9** and their corresponding iodinated compounds **2–5**, used at a final concentration of 10, 1.0, 0.1 or 0.01 μM, to inhibit the binding of M21 melanoma cells to various RGD-containing substrates, such as vitronectin, fibronectin or osteopontin.

The analyses were performed in the presence of 2 mM $MnCl_2$, in order to switch integrins of tumor cells into an activated form. The results shown in Figure 2, panel A, indicated that compound **9** and the iodinated compound **5** did not inhibit melanoma binding to RGD-containing substrates, demonstrating that the alkylation of the guanidine group with tyramine play a detrimental effect towards binding affinity. Compound **6** did not inhibit the binding of M21 melanoma cells to vitronectin and fibronectin, while weakly inhibiting the adhesion to osteopontin when used at a higher dose. The iodinated compound **2**, at the higher dose, weakly inhibited M21 adhesion to fibronectin and osteopontin but not to vitronectin, and the inhibition significantly differed from the non-iodinated compound only in the case adhesion to fibronectin (Fig. 2, panel B). Compounds **7** and **3** inhibited M21 adhesion to vitronectin at the higher doses and the inhibition was completely abolished at lower doses. Also, they inhibited the M21 adhesion to fibronectin and osteopontin at high levels with the higher doses and this inhibition was maintained even when used at lower doses (Fig. 2, panel C). Compounds **8** and **4** expressed an inhibitory ability profile on tumor cell adhesion that is comparable to that of compound **7**. In particular, the iodinated compound **4** showed a significant inhibitory activity on fibronectin and osteopontin adhesion at the lower concentration, as compared to the corresponding non-iodinated compound **8** (Fig. 2, panel D). These results suggest that compounds **6** and **9** and their iodinated analogues **2** and **5**, which do not display a sufficient RGD binding inhibition of tumor cell adhesion, in agreement with competition assay results as reported in Table 1, could not be useful for in vivo analysis. On the contrary, compounds **7** and **8**, which display a quite comparable affinity for the $\alpha_v\beta_3$ integrin receptor, could be used successfully for in vivo imaging studies, due to their inhibitory activity on M21 tumor cell adhesion on RGD substrates. Interestingly, the presence of the iodine atom in **3** and **4** significantly augmented the inhibitory ability of the two compounds on living cells adhesion, in agreement with $\alpha_v\beta_3$ integrin binding assays.

2.4. Molecular modeling

In order to understand the differences in the binding mode of selected iodinated-RGD peptidomimetics **2**, **3** and **4** to $\alpha_v\beta_3$ integrin, a docking simulation was carried out. Compound **5** was not considered for this study having ascertained its poor affinity towards $\alpha_v\beta_3$ integrin. The crystal structure of the complex formed by *c*[RGDf(Me)V], also known as Cilengitide (Fig. 3, red structure), and the extracellular fragment of $\alpha_v\beta_3$ integrin (PDB code: 1L5G) provides a general mode of interaction between the integrin and its ligands.[25]

In particular, Asp carboxylate and Arg guanidinium moieties of RGD mimetic ligands are key structural elements for receptor recognition, which display their binding mode through the carboxylate group interacting with the metal ion-dependent adhesion site (MIDAS) of the Mn^{2+} ion and Ser121/Ser123, and the Arg guanidinium group being responsible for salt bridge interactions with Asp218 and Asp150 side chains. Additional ligand–receptor contacts occur between Tyr122 in hydrophobic π-stacking and Asn215. Autodock 4.0[26] was used for molecular docking calculations to evaluate the binding energies of selected conformations of RGD mimetic ligands **2–4**. Docked conformations were analyzed by taking into account the binding interactions as observed in the crystal structure of the bound ligand–protein complex. Docking calculations of all RGD peptidomimetics **2–4** resulted in a cluster of conformations characterized by key interactions with Asp218 and the MIDAS site of the integrin, thus confirming these interactions being necessary for the molecular recognition of Arg–Gly–Asp-containing ligands (Fig. 3). Specifically, the COOH group was found in the MIDAS site and interacting with Ser121, and the guanidinium group, or its isosteres for **3** and **4**, undergoing a salt-bridge interaction with Asp218 and Asp150.

The main conformation of **2** showed two π-stacking interactions experienced by the D-Tyr aromatic ring facing Tyr-122, and the triazole ring interacting with Tyr178 (Fig. 3, top). This binding profile was in agreement with the ligand properties of Cilengitide with the exception of the characteristic π-stacking interactions between **2** and Tyr178. A different binding mode geometry was assessed for compound **3** as a result of two cation–π interactions[27,28] experienced by Arg214 and the 3′-iodophenol moiety of **3**, and between Tyr178 and the benzimidazole group. The latter interaction replaced the triazole ring in the π-interaction with Tyr178 (Fig. 3, middle). Compound **4** showed a binding mode similar to **2**, consisting of a preferred salt bridge interaction of the 2-aminopyridyl moiety with Asp150 and a compact π-stacking

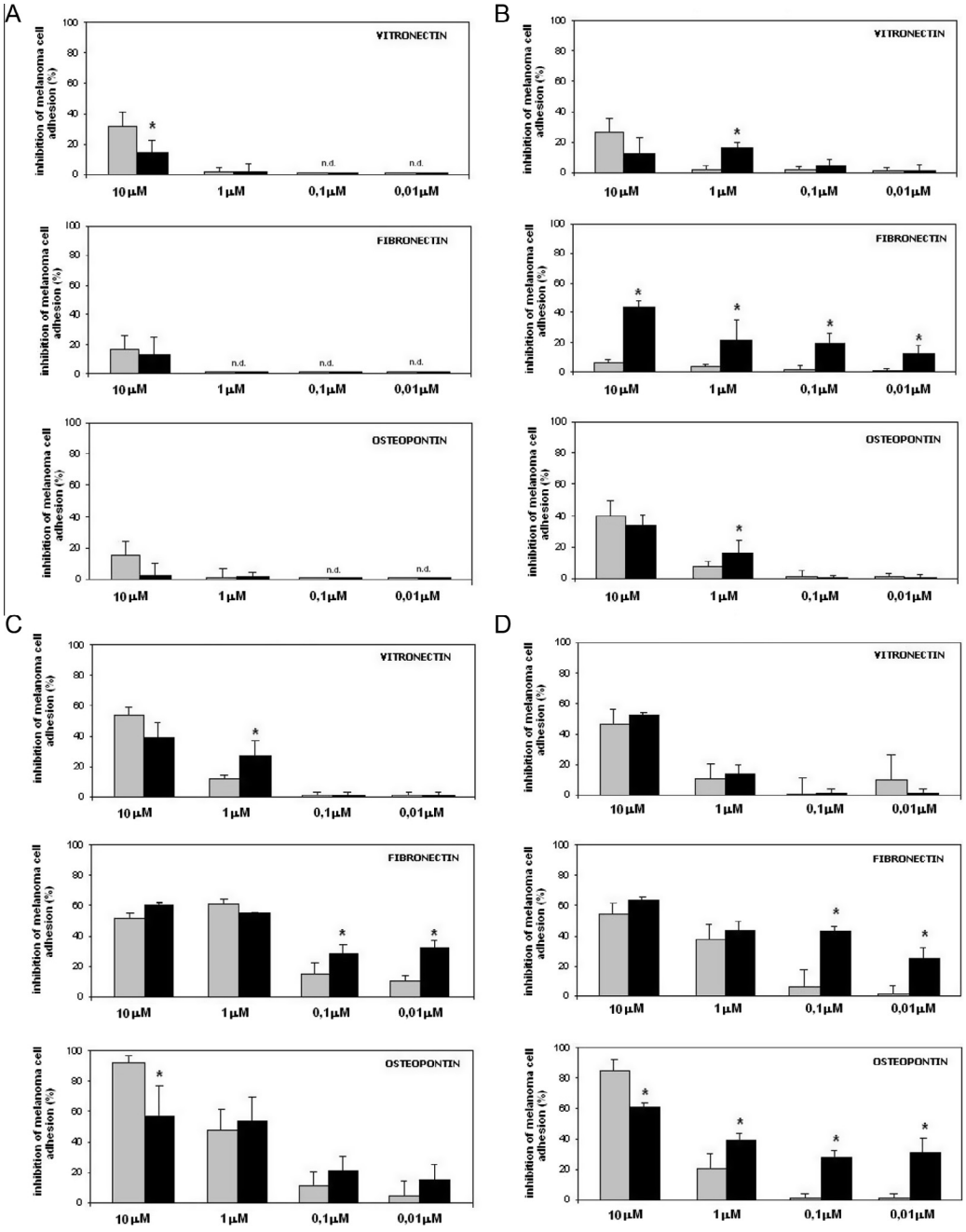

Figure 2. Percentage of inhibition of integrin-mediated M21 cell adhesion to vitronectin, fibronectin and osteopontin, by compounds **9** and **5** (panel A, black and grey, respectively), by compounds **6**, and **2** (panel B, black and grey, respectively), by compounds **7** or **3** (panel C, black and grey, respectively) and by compounds **8** or **4** (panel D, black and grey, respectively). Experiments were conducted in triplicate and repeated at least three times. Data are presented as means ± SEM from three independent experiments, statistical analysis was conducted between the values of the same dose and class of compound, The asterisks indicate a significant difference at $p < 0.05$ as compared to the corresponding non-iodinated compounds.

interaction between the triazole ring and Tyr178 (Fig. 3, bottom). Thus, the modulation of the guanidine isostere proved to affect the binding mode towards $\alpha_v\beta_3$ integrin at the molecular level. Also, the binding mode of **3** and **4** with respect to Cilengitide suggested the interaction with Tyr122 being not crucial for ligand affinity, and showing a different binding asset of the heterocyclic guanidine bioisosteres with respect to Asp218 and Asp150.

2.5. Imaging of melanoma xenografts

Radiolabeling of compounds **6**–**9** was achieved in a solution of PBS containing $Na^{125}I$, and chloramine-T as the oxidizing agent, followed by HPLC purification. Fractions containing the chemically pure ^{125}I-compounds, as determined with a γ-counter, were pooled together (38–49% radiochemical yield) and used for in vivo experiments after solvent removal and solubilization in a physiological saline solution. Biodistribution studies of bioactive ^{125}**I-2**–^{125}**I-4** compounds were performed by micro SPECT-CT imaging. Figure 4, upper panel, shows transaxial slices of tumor bearing mice iv injected with ^{125}**I-2**–^{125}**I-4** compounds, taken at the tumor level. Compound ^{125}**I-5** did not show any activity in vivo either at 30 min post-injection or at later acquisitions, as expected (data not shown). Normalized activity concentration (*nACt*) in different organs has been quantified in the liver and kidneys as most

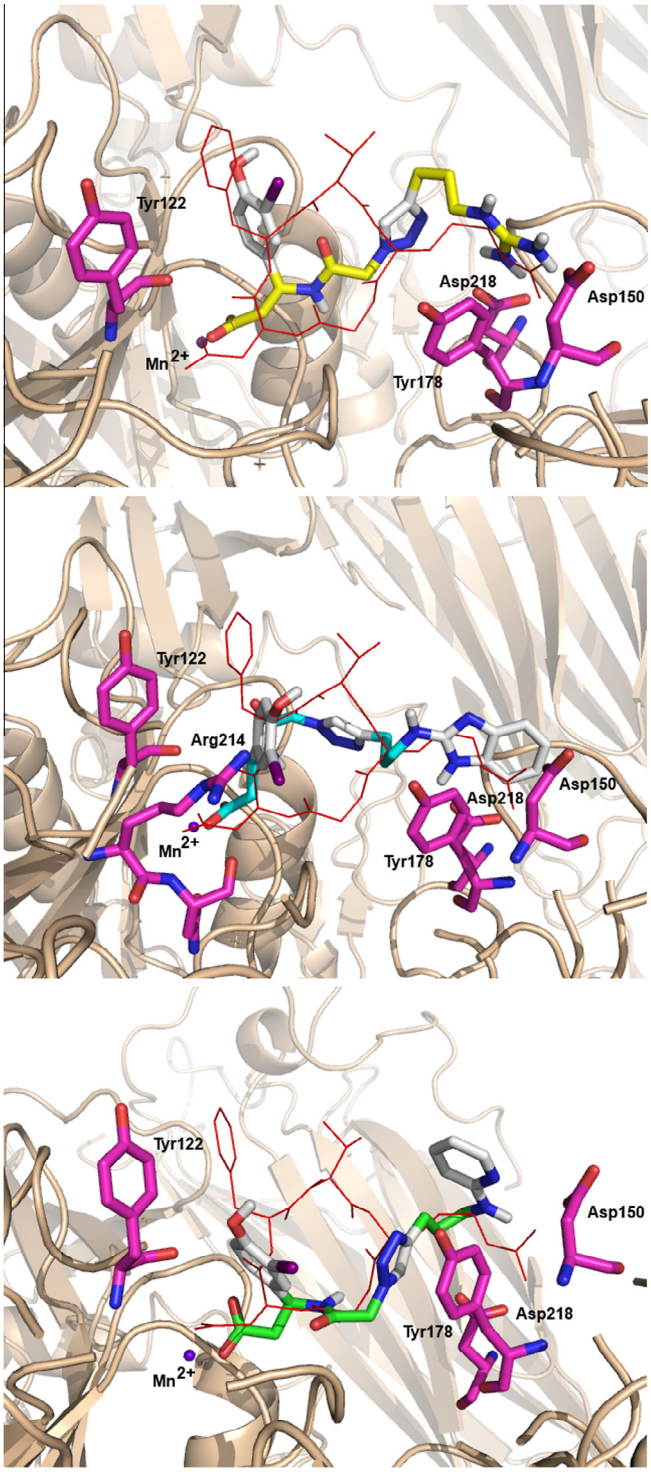

Figure 3. RGD mimetic ligands (top: **2** in yellow, middle: **3** in cyan, bottom: **4** in green) docked into the binding region of $\alpha_v\beta_3$ integrin, highlighting protein residues (magenta) that form key interactions: Asp218/Asp150 versus guanidine or isostere, Mn^{2+} versus COOH group, Tyr122 (compound **2**) or Arg214 (compound **3**) versus 3-I-phenol moiety, Tyr178 and triazole (compounds **2** and **4**) or benzimidazole (compound **3**). Coordinates of reference compound Cilengitide, *c*[RGDf(Me)V] (data from PDB: 1L5G) are shown in red for comparison. Non-polar hydrogen atoms are omitted for clarity.

representative organs of the hepatobiliary and urinary excretion pathways, and in tumor tissue (Fig. 4, lower panel). Bladder was omitted since the organ has a rapid rate of filling and emptying. Compound ^{125}**I-2** showed a sudden distribution which mostly concentrated in the kidneys at 30 min post injection (Fig. 4), while at later acquisitions (60 and 120 min) the activity was almost completely lost. The kinetics of this elimination pathway was found to be extremely rapid. A weak activity was found at 30 min p.i. associated with the tumor, when normalized to muscular tissue was rapidly cleared, as demonstrated by the absence of any activity in the later acquisitions.

Interestingly, the insertion of a benzimidazole as arginine mimetic portion in compound ^{125}**I-3** (Fig. 4), resulted in an increase of activity found in the liver and a significant decrease of activity found in the kidneys, suggesting reduced renal elimination kinetics as compared to compound ^{125}**I-2**, and accounting for a longer persistence in the circulatory system. Finally, the activity associated with the tumor mass was found to increase as compared to compound ^{125}**I-2** during the observation time. Compound ^{125}**I-4** showed a strong involvement of hepatobiliary and renal elimination pathways since these kinetics were similar but more intense compared to those of compound ^{125}**I-3**. Interestingly, compound ^{125}**I-4** showed a faster time-dependent increase of the activity in the tumor mass, which was higher as compared to compound ^{125}**I-3** (Fig. 4). These data were found to be in agreement with their receptor affinity (Table 1) and their behavior in the inhibition of melanoma cells adhesion (Fig. 2). Differences in the metabolic patterns of excretion between compound ^{125}**I-2** and the other two ligands, ^{125}**I-3** and ^{125}**I-4**, were likely related to the arginine mimetic portion, as the presence of the benzimidazole and of the aminopyridine moiety contributed to more lipophilic character and less basic behavior of the molecule, ultimately resulting in a longer circulation time. However, 24 h post-injection animals were analyzed and no significant residual signal was found for any of the radioligands. Compounds ^{125}**I-3** and ^{125}**I-4** reached a significant uptake within the tumor mass when data were normalized to the liver (Table 2), as a key organ of the reticuloendothelial system, due to the low tumor-to-background contrast in the liver.

Displacement experiments were conducted to ascertain the binding specificity of the radiolabeled compounds (Fig. 5). These studies were chosen instead of the simple use of a low expressing $\alpha_v\beta_3$ cell line, since integrins are known to be expressed not only by tumor cells and endothelial cells,[29] but also by other stromal cells such cancer-associated fibroblasts.[30] Hence, saturation with the cold compound would interfere with $\alpha_v\beta_3$ expressing cells of a different origin, thus resulting in a lower background signal and a more reliable evaluation of the binding specificity.

As shown in Figure 5, tumor associated activity in mice injected with compound ^{125}**I-3** was reduced after cold compound pre-treatment. Interestingly, the displacement of compound ^{125}**I-4** by the corresponding cold compound was more significant, suggesting a better in vivo ligand binding specificity.

3. Conclusions

$\alpha_v\beta_3$ integrin-targeted radiotracers are putatively able to reveal the presence of a tumor mass and to monitor the growth and diffusion of tumor cells, and to anticipate the efficacy of an antiangiogenic treatment. Thus, they are of great interest as molecular probes for SPECT and PET molecular imaging. In this view, we developed RGD-peptidomimetics using click chemistry, and a first selection of iodinated molecules was evaluated for their in vitro and in vivo capacity to inhibit the adhesion of human melanoma cells to RGD substrates, such as vitronectin and fibronectin. Molecular modeling calculations suggested a diverse binding modality depending upon the guanidine bioisostere present in the RGD peptidomimetic. Indeed, the optimization of the arginine mimetic portion of the molecule was found crucial in modulating the in vivo profile, and SPECT images clearly showed that three of the four selected ^{125}I-compounds have the capacity to monitor the growth

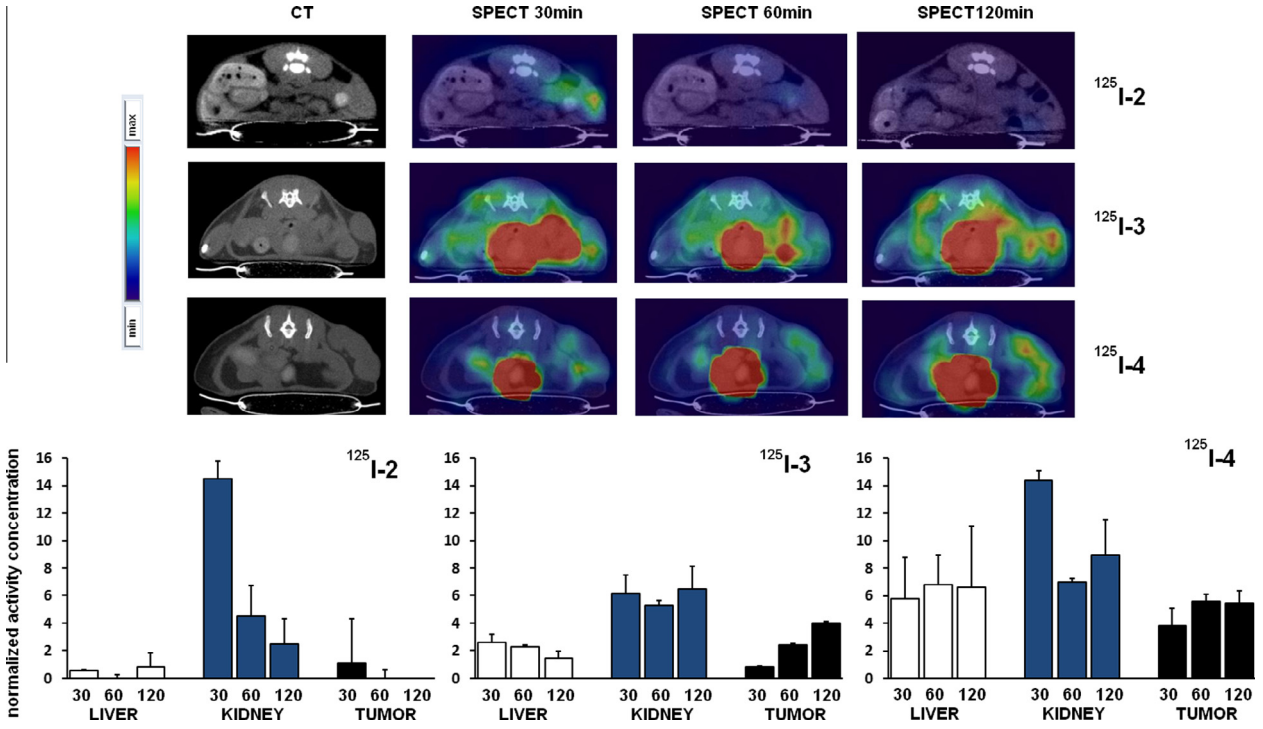

Figure 4. Biodistribution studies of compounds ^{125}**I-2**, ^{125}**I-3**, ^{125}**I-4** in human melanoma xenografts. Upper panel: SPECT/CT transaxial slices taken at the tumor level (arrow) at different time points of observation, representative images of one mouse (n = 3). Co-registered CT images were acquired at 10 min and SPECT images were acquired at 30, 60 and 120 min after tail vein injection of compounds ^{125}**I-2**, ^{125}**I-3**, ^{125}**I-4**, (9.25 MBq in 0.2 mL of saline). Lower panel: distribution analysis of ^{125}**I-2**, ^{125}**I-3**, ^{125}**I-4** in mice at different time points; data are expressed as mean ± SE of different normalized activity concentration (*nACt*) of target tissue from three different animals. The arrows show the area where tumor is present.

Table 2
Uptake efficiency normalized to the liver for compounds ^{125}**I-2**, ^{125}**I-3** and ^{125}**I-4**

	nAC values normalyzed to liver		
	30 min	60 min	120 min
^{125}**I-2**	n.d.	n.d.	n.d.
^{125}**I-3**	n.d.	0.46 ± 0.03	0.54* ± 0.02
^{125}**I-4**	n.d.	0.37 ± 0.05	0.58** ± 0.03

Significantly different (*p <0.05 and **p <0.005).

of a melanoma xenograft. Specifically, we ascertained that benzimidazole and aminopyridine moieties as guanidine bioisosteres produced a rapid uptake in the tumor mass, as evaluated in comparison to background activity in the muscle and in the liver.

Moreover, such compounds resulted in longer permanence of the radiotracer in the tumor tissue. The uptake kinetics of these two compounds in the tumor mass showed an increasing trend, as compared to other radio-halogenated cyclic-RGD peptidomimetic showing a rapid uptake and excretion.[31] The new compounds presented in this study demonstrated a site specific receptor interaction, according to the results obtained in displacement experiments. Nevertheless, compounds ^{125}**I-3** and ^{125}**I-4** will need further investigation and structure refinement in a hit-to-lead process in order to achieve promising RGD peptidomimetic markers for molecular imaging in early detection of cancer lesion and for monitoring the antiangiogenic therapeutic response.

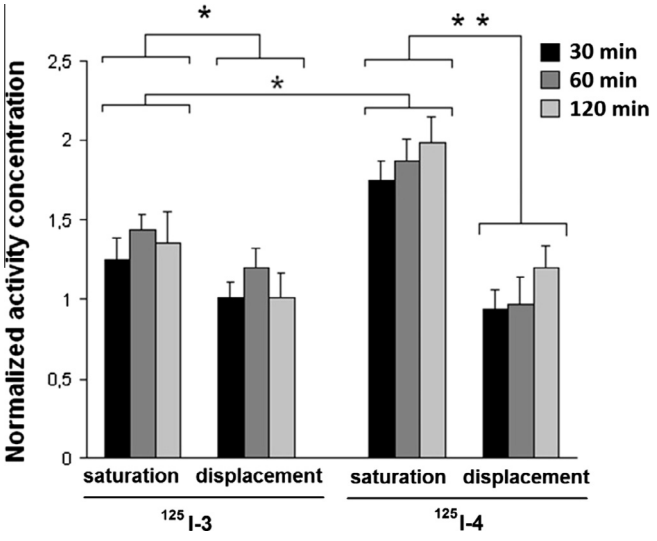

Figure 5. Displacement experiments in tumor bearing mice (n = 3) were performed three days after saturation experiments in the same mice. Displacements were achieved with an excess of the 'cold' ligand (18 mg/kg) injected 10 min before the corresponding radiolabeled tracer. Data are expressed as mean ± SE of different normalized activity concentration (*nACt*) of the target tissue from three different animals at different time points p.i. Discrepancies between *nACt* of different compounds at each time point were significant *p <0.05. Differences between *nACt* of saturation versus displacement were significant at each time point with *p <0.05 for compound ^{125}**I-3** and **p <0.001 for compound ^{125}**I-4**.

4. Experimental section

4.1. General

^{1}H NMR and ^{13}C NMR spectra were recorded on a Varian Gemini 200 or a Varian Gemini 300. Flash column chromatography (FCC) purifications were performed using Merck silica gel (40–63 μm), or via an automated Biotage Isolera system (SNAP silica cartridges). TLC analyses were performed on Merck silica gel 60 F254 plates. Elemental analyses were recorded on a Perkin Elmer 240 CHN

Analyzer. ESI mass spectra were recorded on a Thermo LCQ-Fleet. All commercially available reagents and solvents were purchased from Sigma–Aldrich and used as received, unless otherwise specified. Analytical HPLC purity tests and semipreparative HPLC purifications of radioligands were performed on a Beckman-Coulter System GOLD (column Grace Discovery Sciences Alltima C18 10 μm; 250 × 10 mm), using H_2O/CH_3CN gradient eluant buffered with 0.1% TFA (flow rate 2.5 mL/min, λ = 254 nm, gradient eluant: CH_3CN 10%/5 min, CH_3CN 10–90%/25 min). HPLC analysis was used to determine purity and all tested compounds possessed >95% purity.

4.2. General procedure (A) for the synthesis of RGD mimetic ligands 6–9

Azide (1.1 equiv) was dissolved in THF (0.15 M solution), then alkyne (1 equiv) and $CuP(OEt)_3I$ (0.11 equiv) were added. The reaction was performed under microwave irradiation at 120 °C for 1 h, then THF was evaporated, the crude residue dissolved in EtOAc or DCM, and washed with concentrated ammonia solution and brine. The organic layer was dried over Na_2SO_4, evaporated under vacuum and purified via flash column chromatography. The protected adduct was suspended in 3 M HCl (10 mL/mmol) and stirred at 30 °C overnight. The solution was evaporated to dryness in vacuo to afford the corresponding product in pure form.

4.3. (*S*)-3-(2-(4-(3-Guanidinopropyl)-1*H*-1,2,3-triazol-1-yl)acetamido)-3-(4-hydroxyphenyl)propanoic acid hydrochloride (6)

Following the general procedure (A), the side chain-protected (Pg) **Pg-6** was obtained as a pale yellow oil in 89% yield. The hydrolysis of **Pg-6** allowed us to obtain the final product **6** as a white solid in quantitative yield. ^{1}H NMR (300 MHz, D_2O) δ 7.63 (s, 1H), 7.10 (d, J = 7.8 Hz, 2H), 6.72 (d, J = 7.8 Hz, 2H), 5.2–4.9 (m+s, 3H), 3.02 (t, J = 6.6 Hz, 2H), 2.78–2.75 (m, 2H), 2.63 (t, J = 6.6 Hz, 2H), 1.78 (t, J = 6.6 Hz, 2H). ^{13}C NMR (50 MHz, D_2O) δ 173.6, 165.2, 155.8, 154.3, 130.9, 127, 114.7, 51.9, 49.4, 39.4, 39.1, 26.3, 20.4. ESI-MS m/z 412.3 [$(M+Na)^+$, 66], 390.33 [$(M+H)^+$, 100]. Anal. Calcd for $C_{17}H_{24}ClN_7O_4$: C, 47.94; H, 5.68; N, 23.02. Found: C, 48.11; H, 5.73; N, 22.90. HPLC: t_R = 10.22 min, 98% purity.

4.4. (*S*)-2-((3-(1-(2-((2-Carboxy-1-(4-hydroxyphenyl)ethyl)amino)-2-oxoethyl)-1*H*-1,2,3-triazol-4-yl)propyl)amino)-1*H*-benzo[d]imidazol-3-ium trifluoroacetate (7)

Following the general procedure (A), **Pg-7** was obtained as a colorless oil in 57% yield. Following a different hydrolysis procedure, **Pg-7** (45 mg, 0.06 mmol) was dissolved in 2 mL of a 1:1 mixture of DCM–TFA and stirred at room temperature 2 h. The solvent was evaporated to yield the deprotected product **7** in quantitative yield. ^{1}H NMR (300 MHz, D_2O) δ 7.62 (s, 1H), 7.08–7.03 (s+d, 4+2H), 6.64 (dd, J = 6.6, 2.1 Hz, 2H), 5.08–5.00 (m, 3H), 3.19 (t, J = 6.9 Hz, 2H), 2.76–2.66 (m, 4H), 1.90 (t, J = 6.9 Hz, 2H). ^{13}C NMR (50 MHz, D_2O) δ 173.7, 165.7, 154.1, 149.5, 146.0, 130.9, 128.1, 126.8, 123.9, 122.4, 114.5, 110, 51.3, 49.3, 44.6, 41.0, 39.1, 26.4, 20.7. ESI-MS m/z 464.3 [$(M+H)^+$, 100]. Anal. Calcd for $C_{25}H_{26}F_3N_7O_6$: C, 51.99; H, 4.54; N, 16.98. Found: C, 52.25; H, 4.64; N, 16.79. HPLC: t_R = 15.91 min, 98% purity.

4.5. (*S*)-3-(4-Hydroxyphenyl)-3-(2-(4-(3-(pyridin-2-ylamino)propyl)-1*H*-1,2,3-triazol-1-yl)acetamido)propanoic acid hydrochloride (8)

Following the general procedure (A), **Pg-8** was obtained as a colorless yellow oil in 55% yield. The hydrolysis of **Pg-8** in 3 M HCl allowed us to obtain the final product **8** as a white solid in quantitative yield. ^{1}H NMR (300 MHz, D_2O) δ 7.62 (s, 1H); 7.60–7.56 (m, 1H), 7.52–7.48 (m, 1H), 7.07 (d, J = 8.4 Hz, 2H), 6.71–6.66 (m, 3H), 6.65–6.61 (m, 1H), 5.09–4.95 (m, 3H), 3.16 (t, J = 6.9 Hz, 2H), 2.77–2.73 (m, 2H), 2.67 (t, J = 6.9 Hz, 2H), 1.91–1.81 (m, 2H). ^{13}C NMR (50 MHz, D_2O) δ 173.6, 165.5, 154.1, 151.5, 145.6, 142.3, 133.6, 130.9, 127.9, 126.9, 124.1, 114.6, 112.1, 111.3, 51.5, 49.3, 44.7, 39.7, 39.0, 25.8, 20.6. ESI-MS m/z 425.2 [$(M+H)^+$, 100]. Anal. Calcd for $C_{21}H_{24}N_6O_4$: C, 59.42; H, 5.70; N, 19.80. Found: C, 59.55; H, 5.76; N, 19.66. HPLC: t_R = 12.80 min, 99% purity.

4.6. (*S*)-3-(2-(4-(3-(3-(4-hydroxyphenethyl)guanidino)propyl)-1*H*-1,2,3-triazol-1-yl)acetamido)-3-phenylpropanoic acid hydrochloride (9)

Following the general procedure (A), **Pg-9** was obtained as a colorless oil in 82% yield. The hydrolysis of **Pg-9** in 3 M HCl allowed us to obtain the final product **9** as a white solid in quantitative yield. ^{1}H NMR (300 MHz, D_2O) δ 7.47 (s, 1H), 7.22–7.14 (m, 5H), 6.90 (d, J = 8.4 Hz, 2H), 6.58 (d, J = 8.4 Hz, 2H), 5.15–5.05 (m, 1H), 5.01 (d, J = 3.6 Hz, 2H), 3.19 (t, J = 6.6 Hz, 2H), 2.87 (t, J = 6.6 Hz, 2H), 2.77 (d, J = 6.6 Hz, 2H), 2.55 (t, J = 6.6 Hz, 2H), 2.45 (t, J = 7.2 Hz; 2H), 1.60–1.52 (m, 2H). ^{13}C NMR (50 MHz, $CDCl_3$) δ 174.4, 166.5, 155.5, 154.1, 139.9, 130.2, 129.4, 128.9, 128.1, 127.0, 126.3, 115.4, 52.4, 50.7, 42.3, 40.1, 39.8, 33.5, 27.1, 21.3. ESI-MS m/z 494.4 [$(M+H^+$, 100]. Anal. Calcd for $C_{25}H_{32}ClN_7O_4$: C, 56.65; H, 6.09; N, 18.50. Found: C, 56.73; H, 6.18; N, 18.24. HPLC: t_R = 23.34 min, 98% purity.

4.7. General procedure (B) for the synthesis of 2–4

Deprotected RGD mimetic ligand was dissolved in 1:1 H_2O–MeOH mixture (0.05 M), and NaI (1 equiv), dissolved in the minimum quantity of water, was added to the mixture. Then a solution of chloramine-T, dissolved in the minimum quantity of water, was added and the resulting mixture was stirred for 20 min at rt. Afterwards, an aqueous solution of sodium bisulfite (mixture with metabisulfite, 1 equiv) was added, followed by water addition (starting volume × 4) and the solution was washed with DCM. The aqueous layer was evaporated and aliquots of the mixture were purified via semipreparative HPLC giving suitable quantities of iodinated product for ^{1}H NMR and biological assays.

4.8. (*S*)-Amino((3-(1-(2-((2-carboxy-1-(4-hydroxy-3-iodophenyl)ethyl)amino)-2-oxoethyl)-1*H*-1,2,3-triazol-4-yl)propyl)amino)methaniminium trifluoroacetate (2)

Iodination of compound **6** was achieved according to general procedure (B) as above to give pure **2** after HPLC purification. ^{1}H NMR (300 MHz, D_2O) δ 7.66 (s, 1H), 7.59 (s, 1H), 7.11 (d, J = 8.4 Hz, 2H), 6.79 (d, J = 8.4 Hz, 2H), 5.10–5.03 (m, 3H), 3.04 (t, J = 6.9 Hz, 2H), 2.78 (bd, J = 6.9 Hz, 2H), 2.66 (t, J = 7.2 Hz, 2H), 1.81 (t, J = 7.2 Hz, 2H). ESI-MS m/z 537.5 [$(M+Na)^+$, 100], 516.1 [$(M+H)^+$, 18]. HPLC: t_R = 13.22 min, 97% purity.

4.9. (*S*)-2-((3-(1-(2-((2-Carboxy-1-(4-hydroxy-3-iodophenyl)ethyl)amino)-2-oxoethyl)-1*H*-1,2,3-triazol-4-yl)propyl)amino)-1*H*-benzo[*d*]imidazol-3-ium trifluoroacetate (3)

Iodination of compound **7** was achieved according to general procedure (B) as above to give pure **3** after HPLC purification. ^{1}H NMR (300 MHz, D_2O) δ 7.63 (s, 1H), 7.45 (d, J = 2.1 Hz, 1H), 7.05–6.99 (m, 5H), 6.62 (d, J = 8.7 Hz; 1H), 5.10–4.93 (m, 3H), 3.23–3.10 (m, 2H), 2.71 (t, J = 6.9 Hz, 4H), 1.92 (t, J = 6.9 Hz, 2H). ESI-MS m/z 612.14 [$(M+Na)^+$, 24], 590.16 [$(M+H)^+$, 100]. HPLC: t_R = 17.96 min, 97% purity.

4.10. (*S*)-2-((3-(1-(2-((2-carboxy-1-(4-hydroxy-3-iodophenyl) ethyl)amino)-2-oxoethyl)-1*H*-1,2,3-triazol-4-yl)propyl) amino)pyridin-1-ium trifluoroacetate (4)

Iodination of compound **8** was achieved according to general procedure (B) as above to give pure **4** after HPLC purification. ^{1}H NMR (300 MHz, D_2O) δ 7.62 (s, 1H), 7.59–7.53 (m, 3H), 7.06 (dd, J = 8.1, 2.1 Hz, 1H), 6.70 (d, J = 8.1 Hz, 1H), 6.66–6.58 (m, 3H), 5.05–4.97 (m, 3H), 3.12 (t, J = 6.9 Hz, 2H), 2.76–2.64 (m, 4H), 1.91–1.83 (m, 2H). ESI-MS m/z 551.2 [$(M+1)^+$, 38], 439.3 (100). HPLC: t_R = 14.84 min, 96% purity.

4.11. (*S*)-((3-(1-(2-((2-Carboxy-1-phenylethyl)amino)-2-oxoethyl)-1*H*-1,2,3-triazol-4-yl)propyl)amino)((4-hydroxy-3-iodophenethyl)amino)methaniminium trifluoroacetate (5)

Iodination of compound **9** was achieved according to general procedure (B) as above to give pure **5** after HPLC purification. ^{1}H NMR (300 MHz, D_2O) δ 7.50 (s, 1H), 7.41 (s, 1H), 7.41 (s, 1H), 7.29–7.11 (m, 5H), 6.92 (d, J = 8.4 Hz, 1H), 6.64 (d, J = 8.4 Hz, 1H), 5.15–5.00 (m, 3H), 3.25–3.15 (m, 2H), 2.87 (t, J = 6.9 Hz, 2H), 2.80 (d, J = 6.6 Hz, 2H), 2.60–2.51 (m, 2H), 2.44 (t, J = 6.9 Hz, 2H), 1.58–1.51 (m, 2H). ESI-MS m/z 620.2 [$(M+H)^+$, 100]. HPLC: t_R = 25.34 min, 97% purity.

4.12. Radiolabeling with Na^{125}I

A solution of PBS (100 μL, 0.05 M) containing Na^{125}I (50 μL, 5 mCi, 2.29 nmol), either compound **6**, **7**, **8**, or **9** (10 μL of a 0.05 M PBS solution, 41.2 nmol), and chloramine-T (1.88 μL of a freshly prepared 0.05 M PBS solution, 8.24 nmol) was prepared. The reaction mixture was stirred at room temperature for 20 min and then quenched by adding a solution of sodium metabisulfite (2.18 μL of a freshly prepared 0.05 M PBS solution, 8.24 nmol). The mixture was extracted with DCM (2 × 0.2 mL) and purified by HPLC, and the radioactivity of fractions collected every 30 s was determined with a γ-counter. Fractions containing the chemically pure ^{125}I-compound were pooled together and used for in vivo experiments after solvent removal and solubilization in physiological saline solution (38–49% radiochemical yield). **^{125}I-2**: 49% radiochemical yield, HPLC: t_R = 13.39 min, 99% radiochemical purity; **^{125}I-3**: 41% radiochemical yield, HPLC: t_R = 18.17 min, 99% radiochemical purity; **^{125}I-4**: 38% radiochemical yield, HPLC: t_R = 15.01 min, 99% radiochemical purity; **^{125}I-5**: 48% radiochemical yield, HPLC: t_R = 25.49 min, 99%.

4.13. Solid-phase integrin binding assay

^{125}I-echistatin[32] with a specific activity of 2000 Ci/mmol, was purchased from Perkin Elmer, and integrin $\alpha_v\beta_3$ from human placenta was purchased from Millipore. Purified $\alpha_v\beta_3\alpha_v\beta_3$ integrin was diluted in coating buffer [20 mM Tris (pH 7.4), 150 mM NaCl, 2 mM $CaCl_2$, 1 mM $MgCl_2$, 1 mM $MnCl_2$] at concentrations of 500 or 1000 ng/mL. An aliquot of diluted integrin (100 μL/well) was added to a 96-well microtiter plate (Optiplate-96 HB, PerkinElmer Life Sciences, Boston, MA), and plates were incubated overnight at 4 °C, followed by washings with blocking/binding buffer [20 mM Tris (pH 7.4), 150 mM NaCl, 2 mM $CaCl_2$, 1 mM $MgCl_2$, 1 mM $MnCl_2$, 1% BSA] and incubated at room temperature for additional 2 h. After rinsing twice with the same buffer, competition binding assays were performed with a constant concentration of ^{125}I-echistatin (0.05 nM) and with concentrations of tested compound ranging from 0.01 to 100 nM. All assays were performed in triplicate in a final volume of 0.2 mL, each containing the following species: 0.05 mL of ^{125}I-echistatin, 0.04 mL of tested compound, and 0.11 mL of blocking/binding buffer. Nonspecific binding was defined as ^{125}I-echistatin bound in the presence of an excess (1 μM) of unlabeled echistatin. After incubation at room temperature for 3 h, plates were washed three times with blocking/binding buffer and counted in a Top-Count NXT microplate scintillation counter (PerkinElmer Life Sciences, Boston, MA) using 200 μL/well of MicroScint-40 liquid scintillation (PerkinElmer Life Sciences, Boston, MA). Data are shown as means ± SD from three independent experiments. IC_{50} values were determined by fitting binding inhibition data by nonlinear regression using GraphPad Prism 4.0 Software Package (GraphPad Prism, San Diego, CA). Any possible binding of displaced radioactive ligand to BSA was evaluated in every assay by comparing the total bound value to the total added value as blank controls, resulting in a deviation due to radioligand binding to BSA of about 5%, which may be comprised within the experimental errors.

4.14. Cell lines and culture conditions

The M21 human melanoma cell line was obtained from the American Type Culture Collection (ATCC, Rockville, MD). Melanoma cells were grown in Dulbecco's modified Eagle medium, containing 4500 mg/L glucose (DMEM 4500, GIBCO) supplemented with 10% foetal calf serum (FCS) at 37 °C in a humidified incubator containing 10% CO_2. 5.0×10^5 melanoma cells were seeded in 100 mm Sarstedt dishes and propagated every 3 days by incubation with a trypsin–EDTA solution. Cultures were periodically monitored for mycoplasma contamination. For the use in the experiments, cells (passages 2–4) were grown to confluence in plates coated with 1% bovine gelatin (Sigma, St. Louis).

4.15. Cytofluorimetric assay

Cells were detached by gentle treatment with Accutase (Lonza), a 0.5 mM EDTA solution, washed, and incubated for 1 h at 4 °C in the presence of anti-$\alpha_v\beta_3$ monoclonal antibody (1 μg/50 μL, anti-integrin $\alpha_v\beta_3$, clone LM609, Millipore) and anti-$\alpha_v\beta_5$ monoclonal antibody (1 μg/50 μL, anti-integrin $\alpha_v\beta_5$, Santa Cruz 13588). Cells were then washed and incubated for 1 h at 4 °C with a specific secondary antibody, 5 μg/mL goat antimouse IgG conjugated with FITC (Santa Cruz Biotechnology, Inc., Santa Cruz, CA). Integrin-Positive cells were analyzed at 488 nm on the flow cytometer FACScan system (BD-FACS Canto).

4.16. Cell adhesion assay

Plates (96 wells) were coated with vitronectin (10 μg/mL), osteopontin (0.5 μg/mL) or fibronectin (1 μg/mL), by overnight incubation at 4 °C. Plates were washed with PBS and then incubated at 37 °C for 1 h with PBS–1% BSA. After being washed tumor cells were counted and resuspended in serum free medium, and exposed to compound (final concentration was 10 nM, 0.1, 1, or 10 μM) at 37 °C for 30 min to allow the ligand–receptor equilibrium to be reached. Assays were performed in the presence of 2 mmol/L $MnCl_2$. Cells were then plated ($4–5 \times 10^4$ cells/well) and incubated at 37 °C for 1 h. All the wells were washed with PBS to remove the non adherent cells, and 0.5% crystal violet solution in 20% methanol was added. After 2 h of incubation at 4 °C, plates were examined at 540 nm in a counter ELX800 (Bio TEK Instruments). Experiments were conducted in triplicate and were repeated at least three times. The values are expressed as% inhibition ± SEM of cell adhesion relative to untreated cells.

4.17. Small-animal SPECT and CT studies

The in vivo studies were conducted using a FLEX™ Triumph™ Pre-Clinical Imaging System (Trifoil-Imaging, Northridge, CA). The

engrafted tumor tracer uptake was studied at different time-points (at 30, 60 and 120 min p.i.) after tail vein injection. In vivo experiments were conducted in accordance with national guidelines and approved by the ethical committee of Animal Welfare Office of Italian Work Ministry and in agreement with the legal mandates and Italian guidelines for the care and maintenance of laboratory animals. Eight-ten week-old male SCID bg/bg mice (Charles River Laboratories International) were kept under anesthesia and injected subcutaneously with a suspension mixture of 1×10^6 M21 melanoma cells resuspended in 100 μL of PBS diluted 1:1 with a Matrigel solution (BD Biosciences). Animals were kept under pathogen-free conditions and allowed to feed freely. Tumor growth was monitored every other day. Saturation experiments were performed in order to visualize grafted tumors. ^{125}I-compounds (each radiolabeled with 0.2–0.3 mCi in 200 μL of physiological saline solution) were injected in the tail vein of tumor bearing mice kept under isoflurane anesthesia. CT scan was performed followed by the SPECT tomography at 30 min p.i. with animals being kept under anesthesia on a warmed bed and monitoring for breath frequency. Animals were ip injected with 150 μL of a solution of KI (4 mg/L) 1 h before injection of the different compounds to avoid the accumulation in the thyroid gland of the ^{125}I atom possibly released from the molecule. The CT scan was acquired with 50 kV and 320 μA tube settings. The magnification factor was set to 2 resulting in an axial field of view of 59.2 mm. 512 projections, 500 μs each, were acquired on a circular orbit in 256 s with an acquisition matrix of 1184 × 1120, 115.6 μm pixel size. Having the animal bed in the same position, 64 SPECT projections (20 s each) were acquired on a circular orbit with radius of rotation of 40 mm and a 5-pinhole high-resolution collimator (1 mm hole diameter, 75 mm focal distance) for a total acquisition time of about 22 min. The acquisition matrix was 80 × 80, 1.5 mm pixel size. The energy window was set on the ^{125}I photopeak ranging from 20 keV and 36 keV. Once the scanning session was complete, animals were recovered in a housing unit and monitored until awake.

4.18. Data analysis of small-animal SPECT and CT studies

The CT image data set was reconstructed using FBP (Filtered Back Projection) algorithm implementing an apodization low pass filter devoted to statistical noise minimization. The reconstruction matrix was 512 × 512 × 512, 180 μm pixel size. SPECT images were reconstructed with OSEM (Ordered Subset Expectation Maximization) algorithm (8 subsets and 5 iterations) and a reconstruction matrix of 60 × 60 × 60, 1.5 mm pixel size. The fused images were visually inspected to detect regional SPECT activities and measured using the analysis software Vivid (Gamma Medica-Ideas, Northridge, CA). Elliptical ROIs (Regions Of Interest) were delineated by hand corresponding to a volume of approximately 0.3–0.5 mL for each organ. Absolute activity concentration in the target (the tumor or the organ) (*AACt*) and in the reference region (*AACr*) (muscular tissue) were measured.[33] Data were also decay-corrected to the time of injection and residual activity in the syringe. Finally, *AAC* data for each organ were normalized to activity (*nACt*) in muscular tissue and corrected for background activity according to the formula:

$$nACt = \frac{AACt - AACr}{AACr}$$

where *nACt* is normalized activity concentration in target tissue, *AACt* and *ACCr* are the absolute activity concentrations of the target tissue and of the reference tissue respectively.

The biodistribution data expressed as *nACt* ratios are reported as mean plus SEM based on the results from three animals at each time point. Comparison between two different radiotracers for DE was also made using the multiple-comparison Student–Newman–Keuls test, after demonstration of significant differences among medians by non-parametric variance analysis, according to the Kruskal–Wallis test. The level of significance was set at $p < 0.05$.

4.19. Docking calculations

Automated docking studies were carried out using the Lamarckian Genetic Algorithm (LGA) as a search engine implemented in the Autodock 4.0.1 program.[26] The AutoDockTools 1.4.5 (ADT) graphical interface[34] was used to prepare integrin and ligands PDBQT files. Coordinates of RGD mimetic ligands **2**–**4** were generated using Spartan (version 5.147), and then energy-minimized through the AM1 semi-empirical method to calculate the equilibrium geometry. The coordinates of $\alpha_v\beta_3$ receptor were retrieved from the Protein Data Bank (PDB code: 1L5G), and ligand–protein complex was unmerged for achieving free receptor structure. Water molecules were removed. For protein receptor and RGD mimetic ligands **2**–**4**, all hydrogen atoms were added, Gasteiger charges were computed, and nonpolar hydrogen atoms were merged. A charge value of +2.0 to each Mn atom of protein receptor was successively added. Three-dimensional energy scoring grids of 0.375 Å resolution and 40 × 40 × 40 Å dimensions were computed. The center of the grid was set to be coincident with mass center of ligands preliminary fitted on the X-ray structure of *c*[RGDf(Me)V] in the $\alpha_v\beta_3$ complex (1L5G). A total of 50 runs with a maximum of 2,500,000 energy evaluations were carried out for each ligand, using the default parameters for LGA. Cluster analysis was performed on docked results using a root–mean–square (rms) tolerance of 1.5 Å. Analysis of the binding mode, calculation of the binding energy, and prediction of the binding activity of docked conformations were carried out using Autodock plugin within PyMol software.[35]

Acknowledgments

Giannetto Comis is acknowledged for technical assistantship on the use of MicroPET/SPECT/CT instrumentation. Financial support from University of Florence, Istituto Toscano Tumori, and MIUR PRIN2010-2011, cod. 2010NRREPL, and Regione Toscana Regional Council through POR CRO FSE 2007–2013 and UNIFI_FSE2012 funding actions is acknowledged. Ente Cassa di Risparmio is acknowledged for financing the MicroPET/SPECT/CT instrument and the Ente CRF grant (2012.0302) entitled 'Melanoma a cattiva prognosi: basi biologiche e possibili ricadute in termini di salute pubblica e progettazione di biofarmaci'.

Supplementary data

Supplementary data associated with this article can be found, in the online version, at http://dx.doi.org/10.1016/j.bmc.2014.12.065.

References and notes

1. Weissleder, R. *Science* **2006**, *312*, 1168.
2. Franc, B. L.; Acton, P. D.; Mari, C.; Hasegawa, B. H. *J. Nucl. Med.* **2008**, *49*, 1651.
3. Gomes, C. M.; Abrunhosa, A. J.; Ramos, P.; Pauwels, E. K. *Adv. Drug Delivery Rev.* **2011**, *63*, 547.
4. Willmann, J. K.; van Bruggen, N.; Dinkelborg, L. M.; Gambhir, S. S. *Nat. Rev. Drug Disc.* **2008**, *7*, 591.
5. Wong, D. F.; Tauscher, J.; Gründer, G. *Neuropsychopharmacology* **2009**, *34*, 187.
6. Van Dort, M. E.; Rehemtulla, A.; Ross, B. D. *Curr. Comput. Aided Drug Des.* **2008**, *4*, 46.
7. Cabodi, S.; del Pilar Camacho-Leal, M.; Di Stefano, P.; Defilippi, P. *Nat. Rev. Cancer* **2010**, *10*, 858.
8. Shattil, S. J.; Kim, C.; Ginsberg, M. H. *Nat. Rev. Mol. Cell. Biol.* **2010**, *11*, 288.
9. Desgrosellier, J. S.; Cheresh, D. A. *Nat. Rev. Cancer* **2010**, *10*, 9.

10. Arnaout, M. A.; Mahalingam, B.; Xiong, J. P. *Annu. Rev. Cell Dev. Biol.* **2005**, *21*, 381.
11. Schottelius, M.; Laufer, B.; Kessler, H.; Wester, H. J. *Acc. Chem. Res.* **2009**, *42*, 969.
12. Onthank, D. C.; Liu, S.; Silva, P. J.; Barrett, J. A.; Harris, T. D.; Robinson, S. P.; Scott Edwards, D. *Bioconjugate Chem.* **2004**, *15*, 235.
13. Jang, B. S.; Lim, E.; Hee Park, S.; Shin, I. S.; Danthi, S. N.; Hwang, I. S.; Le, N.; Yu, S.; Xie, J.; Li, K. C.; Carrasquillo, J. A.; Paik, C. H. *Nucl. Med. Biol.* **2007**, *34*, 363.
14. Neubauer, S.; Rechenmacher, F.; Beer, A. J.; Curnis, F.; Pohle, K.; D'Alessandria, C.; Wester, H.-J.; Reuning, U.; Corti, A.; Schwaiger, M.; Kessler, H. *Angew. Chem., Int. Ed.* **2013**, *52*, 11656.
15. Monaco, A.; Michelin, O.; Prior, J.; Rüegg, C.; Scapozza, L.; Seimbille, Y. *J. Label Compd. Radiopharm.* **2014**, *57*, 365.
16. Cini, N.; Trabocchi, A.; Menchi, G.; Bottoncetti, A.; Raspanti, S.; Pupi, A.; Guarna, A. *Bioorg. Med. Chem.* **2009**, *17*, 1542.
17. Sladojevich, F.; Trabocchi, A.; Guarna, A. *J. Org. Chem.* **2007**, *72*, 4254.
18. Bianchini, F.; Cini, N.; Trabocchi, A.; Bottoncetti, A.; Raspanti, S.; Vanzi, E.; Menchi, G.; Guarna, A.; Pupi, A.; Calorini, L. *J. Med. Chem.* **2012**, *55*, 5024.
19. Trabocchi, A.; Menchi, G.; Cini, N.; Bianchini, F.; Raspanti, S.; Bottoncetti, A.; Pupi, A.; Calorini, L.; Guarna, A. *J. Med. Chem.* **2010**, *53*, 7119.
20. Dijkgraaf, I.; Kruijtzer, J. A.; Frielink, C.; Soede, A. C.; Hilbers, H. W.; Oyen, W. J.; Corstens, F. H.; Liskamp, R. M.; Boerman, O. C. *Nucl. Med. Biol.* **2006**, *33*, 953.
21. Zanardi, F.; Burreddu, P.; Rassu, G.; Auzzas, L.; Battistini, L.; Curti, C.; Sartori, A.; Nicastro, G.; Menchi, G.; Cini, N.; Bottoncetti, A.; Raspanti, S.; Casiraghi, G. *J. Med. Chem.* **2008**, *51*, 1771.
22. Takagi, J.; Petre, B. M.; Walz, T.; Springer, T. *Cell* **2002**, *110*, 599.
23. Humphries, M. J.; McEwan, P. A.; Barton, S. J.; Buckley, P. A.; Bella, J.; Mould, A. P. *Trends Biochem. Sci.* **2003**, *28*, 313.
24. Shimaoka, M.; Springer, T. A. *Nat. Rev. Drug Disc.* **2003**, *2*, 703.
25. Xiong, J. P.; Stehle, T.; Zhang, R.; Joachimiak, A.; Frech, M.; Goodman, S. L.; Arnaout, M. A. *Science* **2002**, *296*, 151.
26. Morris, G. M.; Goodsell, D. S.; Halliday, R. S.; Huey, R.; Hart, W. E.; Belew, R. K.; Olson, A. J. *J. Comput. Chem.* **1998**, *19*, 1639.
27. Zacharias, N.; Dougherty, D. A. *Trends Pharmacol. Sci.* **2002**, *23*, 281.
28. Gallivan, J. P.; Dougherty, D. A. *Proc. Natl. Acad. Sci. U.S.A.* **1999**, *96*, 9459.
29. Weis, S. M.; Cheresh, D. A. *Cold Spring Harb. Perspect. Med.* **2011**, *1*, a006478.
30. Calorini, L.; Bianchini, F. *Cell Commun. Signal.* **2010**, *8*, 24.
31. Haubner, R.; Wester, H. J.; Weber, W. A.; Mang, C.; Ziegler, S. I.; Goodman, S. L.; Senekowitsch-Schmidtke, R.; Kessler, H.; Schwaiger, M. *Cancer Res.* **2001**, *61*, 1781.
32. Kumar, C. C.; Nie, H.; Armstrong, L.; Zhang, R.; Vijay-Kumar, S.; Tsarbopoulos, A. *FEBS Lett.* **1998**, *429*, 239.
33. Israel, O.; Front, D.; Hardoff, R.; Ish-Shalom, S.; Jerushalmi, J.; Kolodny, G. M. *J. Nucl. Med.* **1991**, *32*, 1157.
34. Gillet, A.; Sanner, M.; Stoffler, D.; Olson, A. *Structure* **2005**, *13*, 483.
35. DeLano, W. L. The PyMOL Molecular Graphics System, Schrödinger, LLC (http://www.pymol.org).